nature energy

ARTICLES

https://doi.org/10.1038/s41560-019-0388-0

Building aqueous K-ion batteries for energy storage

Liwei Jiang[1,2], Yaxiang Lu[1*], Chenglong Zhao[1,2], Lilu Liu[1], Jienan Zhang[1], Qiangqiang Zhang[1,2], Xing Shen[3], Junmei Zhao[3], Xiqian Yu[1], Hong Li[1,4], Xuejie Huang[1], Liquan Chen[1] and Yong-Sheng Hu[1,2,4*]

Aqueous K-ion batteries (AKIBs) are promising candidates for grid-scale energy storage due to their inherent safety and low cost. However, full AKIBs have not yet been reported due to the limited availability of suitable electrodes and electrolytes. Here we propose an AKIB system consisting of an Fe-substituted Mn-rich Prussian blue $K_xFe_yMn_{1-y}[Fe(CN)_6]_w{\cdot}zH_2O$ cathode, an organic 3,4,9,10-perylenetetracarboxylic diimide anode and a 22 M KCF_3SO_3 water-in-salt electrolyte. The cathode achieves 70% capacity retention at 100 *C* and a lifespan of over 10,000 cycles due to the mitigation of phase transitions by Fe substitution. Meanwhile, the electrolyte can help decrease the dissolution of both electrodes owing to the lack of free water. The AKIB exhibits a high energy density of 80 Wh kg^{-1} and can operate well at rates of 0.1–20 *C* and over a wide temperature range (−20 to 60 °C). We believe that our demonstration could pave the way for practical applications of AKIBs for grid-scale energy storage.

Grid energy storage technologies are indispensable for the efficient integration of intermittent renewable energies into the grid[1]. Among various energy storage technologies, electrochemical energy storage employing rechargeable batteries is one of the most effective approaches[2]. Owing to their inherent safety and non-toxicity, aqueous rechargeable batteries based on alkali-ion intercalation are promising technologies[3], among which the K^+-based system possesses overall advantages due to its higher abundance compared with that of its Li counterpart and because of its lower standard redox potential (−2.93 V versus standard hydrogen electrode) compared with that of its Na counterpart (−2.71 V versus standard hydrogen electrode)[4,5]. Moreover, K^+-based electrolytes exhibit much higher ionic conductivity due to the smaller Stokes radius of solvated K ions, which enables an ultrahigh-rate capability of K^+ intercalation electrodes[6]. However, to the best of our knowledge, no full aqueous K-ion battery (AKIB) system has been reported yet due to the limited electrodes and electrolytes.

Among cathode candidates, Prussian blue analogues (PBAs) are promising due to their high stability against water and facile tailoring of physicochemical and electrochemical properties[7]. Various PBA cathodes have been reported in AKIBs, but none of them yet exhibits fully satisfactory properties. For example, $K_{0.6}Ni_{1.2}Fe(CN)_6{\cdot}3.6H_2O$ and $K_{0.71}Cu[Fe(CN)_6]_{0.72}{\cdot}3.7H_2O$ electrodes with a long lifespan (5,000–40,000 cycles) have been reported[8,9], but they exhibited a low capacity of about 60 mAh g^{-1}. $K_2FeFe(CN)_6{\cdot}2H_2O$ can offer a higher capacity of 120 mAh g^{-1}, but its lifespan is only about 500 cycles[10]. Among anode options, no promising material has been proposed so far due to the lack of candidates with appropriate redox potential[4–6]. Regarding electrolytes, water-in-salt (WIS) electrolytes, in which dissolved salts outnumber water by both mass and volume, resulting in extremely high-concentration solutions, possess wide voltage windows and appear as suitable candidates for high-voltage aqueous batteries[11]. The previously reported potassium acetate-based WIS electrolyte can display a wide voltage window[12], but the alkaline nature of the electrolyte (pH = 9) is incompatible with many electrodes such as PBA materials[13]. Therefore, exploration of a novel K^+-based WIS electrolyte with high electrode compatibility is of paramount importance.

In this work, we propose a full AKIB fabricated with an Fe-substituted Mn-rich PBA $K_xFe_yMn_{1-y}[Fe(CN)_6]_w{\cdot}zH_2O$ cathode, organic 3,4,9,10-perylenetetracarboxylic diimide (PTCDI) anode and 22 M KCF_3SO_3 WIS electrolyte. The AKIB exhibits a high energy density of 80 Wh kg^{-1} and superior capacity retention of 85% at 20 *C* as well as good cycling stability with 73% capacity retention over 2,000 cycles at 4 *C*. Moreover, the assembled 11 mAh pouch cell also demonstrates superior performance at low rates (0.1 *C*/0.5 *C*) and a wide range of temperatures (−20 to 60 °C). The impressive performances achieved are attributed to the synergistic contributions from the proposed electrodes and electrolyte, whose structure, physicochemical properties, electrochemical behaviour and storage mechanism are systematically studied by many advanced techniques together with first-principles calculations.

Structure and performance of designed cathodes

X-ray diffraction (XRD) patterns and the refined results for the as-prepared $K_xFe_yMn_{1-y}[Fe(CN)_6]_w{\cdot}zH_2O$ samples ($y = 0$, 0.2, 0.35 and 0.5 represent KMnHCF, KFeMnHCF-28, KFeMnHCF-3565 and KFeMnHCF-55, respectively) show a monoclinic phase with a space group of $P2_1/n$ (Fig. 1a, Supplementary Fig. 1a,b and Supplementary Tables 1 and 2), whose crystal structure is displayed in Fig. 1b, showing a typical open framework structure with N-coordinated Mn or Fe cations and C-coordinated Fe cations. The scanning electron microscopy and transmission electron microscopy images of KMnHCF and KFeMnHCF-3565 samples (inset of Fig. 1a and Supplementary Fig. 2a–c) indicate that both samples possess a cubic morphology with edge length of 200–800 nm. The molecular formulae

[1]Key Laboratory for Renewable Energy, Beijing Key Laboratory for New Energy Materials and Devices, Beijing National Laboratory for Condensed Matter Physics, Institute of Physics, Chinese Academy of Sciences, Beijing, China. [2]Center of Materials Science and Optoelectronics Engineering, University of Chinese Academy of Sciences, Beijing, China. [3]Key Laboratory of Green Process and Engineering, Institute of Process Engineering, Chinese Academy of Sciences, Beijing, China. [4]Yangtze River Delta Physics Research Center Co. Ltd, Liyang, China. *e-mail: yxlu@iphy.ac.cn; yshu@iphy.ac.cn

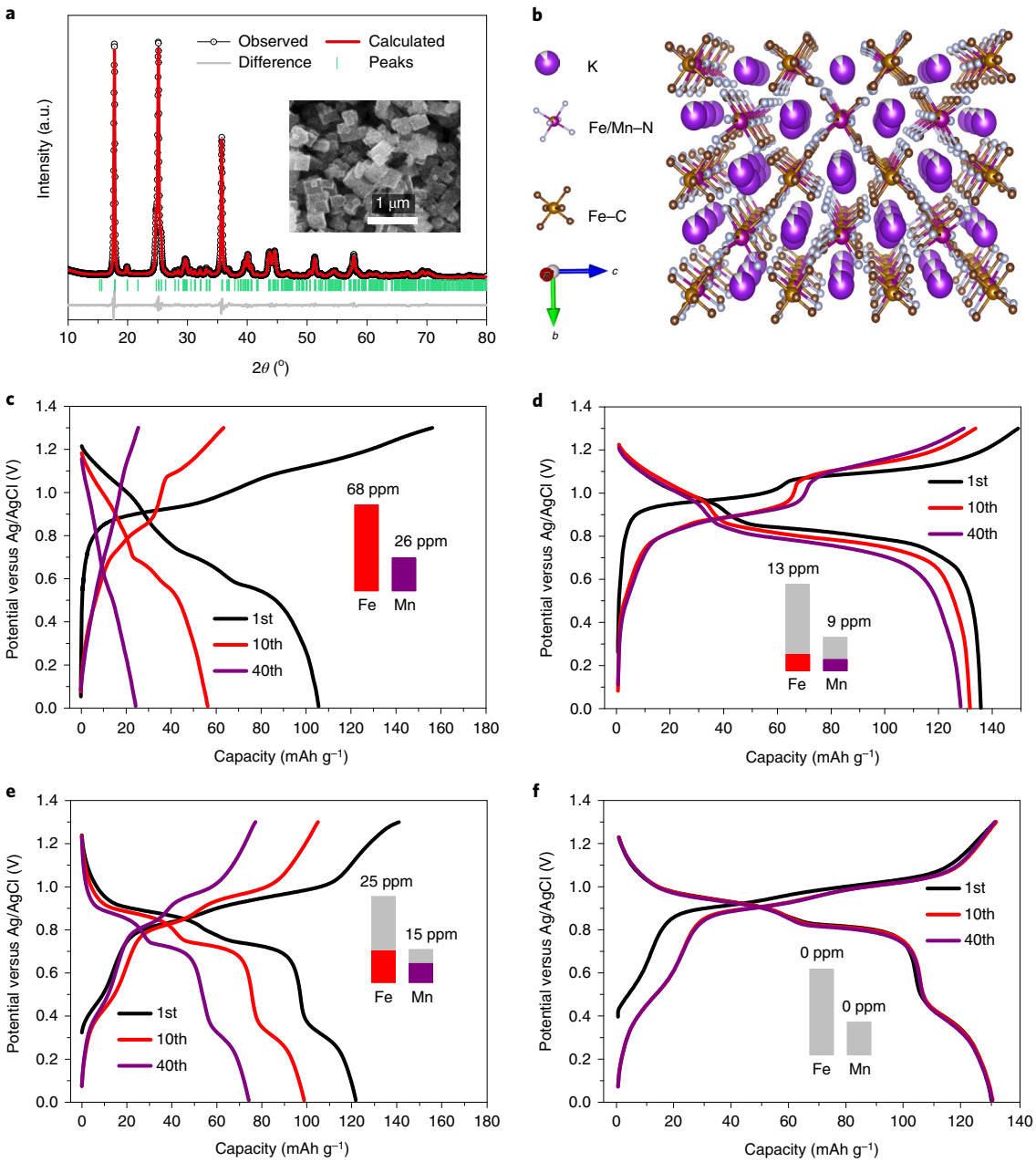

Fig. 1 | The structure and performance optimization of the designed PBA cathodes. a, XRD Rietveld refinement pattern for the KFeMnHCF-3565 sample. The inset is a typical scanning electron microscopy image of the KFeMnHCF-3565 sample. **b**, The typical structure of the $K_xFe_yMn_{1-y}[Fe(CN)_6]_w{\cdot}zH_2O$ in the *P*21/*n* space group. **c**–**f**, Charge–discharge curves of the 1st, 10th and 40th cycles at 10 *C* from 0 V to 1.3 V (versus Ag/AgCl) for the KMnHCF electrode in the 1 M KCF_3SO_3 electrolyte (**c**), the KMnHCF electrode in the 22 M KCF_3SO_3 electrolyte (**d**), the KFeMnHCF-3565 electrode in the 1 M KCF_3SO_3 electrolyte (**e**) and the KFeMnHCF-3565 electrode in the 22 M KCF_3SO_3 electrolyte (**f**). All tests were performed in three-electrode cells with 4 ml aqueous electrolyte. The insets show the dissolved amounts (ppm, mg l^{-1}) of the transition metal ions (Fe and Mn) after 40 cycles in 4 ml of the corresponding electrolyte.

of as-prepared KMnHCF and KFeMnHCF-3565 are determined to be $K_{1.99}Mn[Fe(CN)_6]_{0.94}{\cdot}0.57H_2O$ and $K_{1.85}Fe_{0.33}Mn_{0.67}[Fe(CN)_6]_{0.98}{\cdot}0.77H_2O$, respectively (Supplementary Tables 3 and 4 and Supplementary Fig. 3), with a lower $Fe(CN)_6$ defect in the latter.

Figure 1c–f displays the electrochemical behaviour of KMnHCF and KFeMnHCF-3565 electrodes in the 1 M KCF_3SO_3 dilute electrolyte and 22 M KCF_3SO_3 concentrated electrolyte. The KMnHCF electrode undergoes a rapid decay with only 23% capacity retention at 10 *C* after 40 cycles in the 1 M KCF_3SO_3 electrolyte, while the KFeMnHCF-3565 electrode can retain 60% capacity under the same test conditions. When the electrolyte concentration increases from 1 M to 22 M, the KMnHCF electrode exhibits improved cycling stability but still suffers from capacity and voltage decay. By contrast, the KFeMnHCF-3565 electrode does not exhibit any capacity or voltage decay within the initial 40 cycles. The elemental analysis results of the electrolytes after 40 cycles shown in the insets confirm that the KMnHCF electrode experiences a severe dissolution of Fe and Mn during cycling in dilute electrolyte and undergoes a decreased dissolution in the concentrated electrolyte. In comparison, the KFeMnHCF-3565 electrode displays much less dissolution in dilute electrolyte and does not show any dissolution in concentrated electrolyte, indicating that it is important

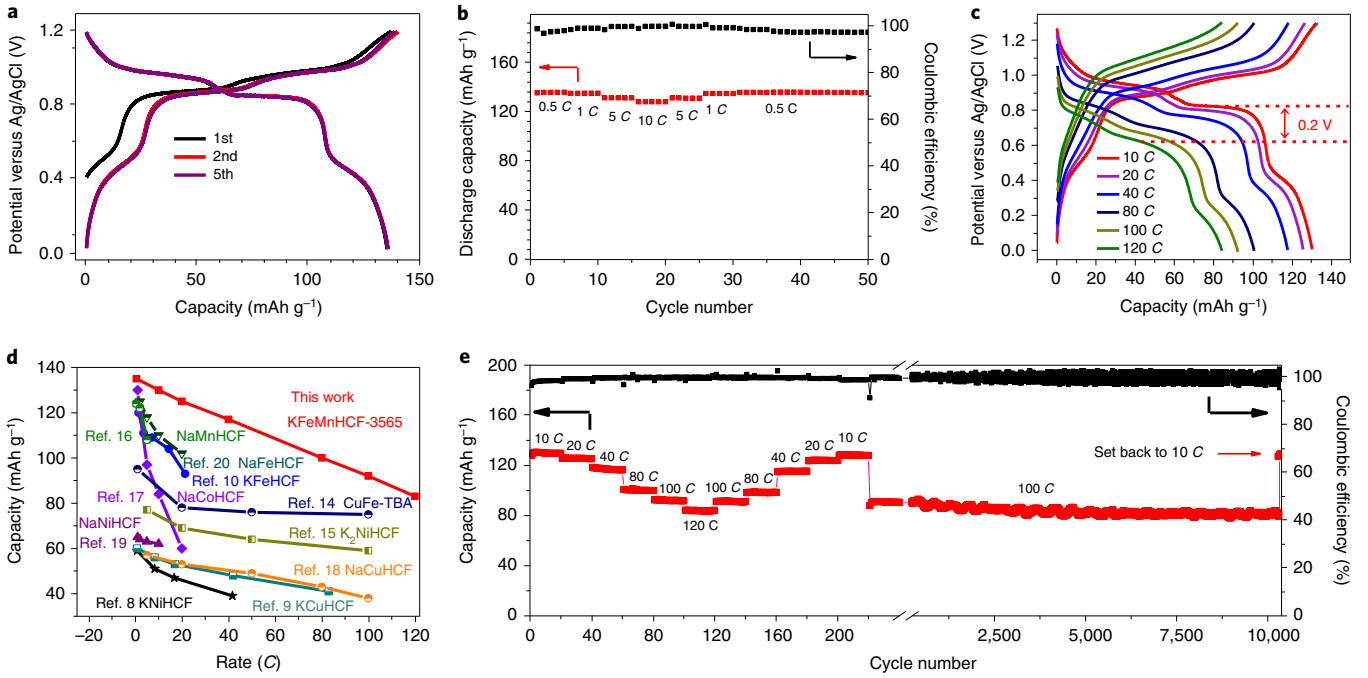

Fig. 2 | Electrochemical performance of the optimal KFeMnHCF-3565 cathode. a, The 1st, 2nd and 5th charge–discharge curves of the KFeMnHCF-3565 electrode at 0.5 *C* from 0 V to 1.2 V (versus Ag/AgCl) in 22 M KCF_3SO_3 electrolyte. **b**, Rate capability at various current rates and the corresponding Coulombic efficiency of the KFeMnHCF-3565 electrode from 0 V to 1.2 V (versus Ag/AgCl) in the 22 M KCF_3SO_3 electrolyte. **c**, Typical charge–discharge curves of the KMnHCF-3565 electrode at different current rates (10–120 *C*). The discharge overpotential from 10 *C* to 120 *C* is marked with red dashed lines. **d**, Capacity versus current rate for PBA cathodes reported in aqueous $K^+/Na^+/H^+$-ion batteries. **e**, Rate capability and long-term cycling performance of the KFeMnHCF-3565 electrode from 0 V to 1.3 V (versus Ag/AgCl) in the 22 M KCF_3SO_3 electrolyte. The mass loading of the KFeMnHCF-3565 cathode is 5.8 mg cm^{-2}, 1 *C* = 0.13 A g^{-1}.

to adopt both Fe substitution and highly concentrated electrolyte. The cycle performance of as-prepared $K_xFe_yMn_{1y}[Fe(CN)_6]_w{\cdot}zH_2O$ (y = 0, 0.2, 0.35. 0.5) electrodes is evaluated in the 22 M KCF_3SO_3 electrolyte (Supplementary Fig. 4a,b), which clearly demonstrates that Fe substitution slightly decreases the capacity and average voltage, but remarkably improves the cycling stability. Among different Fe-substituted electrodes, the KFeMnHCF-3565 electrode shows the optimum overall performance in terms of both capacity and cycling stability, and is chosen for further investigations.

Figure 2a presents the first, second and fifth charge–discharge curves of the KFeMnHCF-3565 electrode at 0.5 *C* from 0 V to 1.2 V (versus Ag/AgCl) in the 22 M KCF_3SO_3 electrolyte, exhibiting a high capacity of 135 mAh g^{-1}. Meanwhile, the KFeMnHCF-3565 electrode exhibits a high capacity retention of 95% at 20 *C* and superior cycling stability when the current rate is set back to 0.5 *C*, as shown in Fig. 2b. Moreover, it displays outstanding high-rate (10–120 *C*) capability (Fig. 2c), which is clearly superior to that of the KMnHCF electrode (Supplementary Fig. 5a,b). In particular, the KFeMnHCF-3565 electrode shows a capacity of 130 mAh g^{-1} at 10 *C* from 0 V to 1.3 V (versus Ag/AgCl) and still retains 85 mAh g^{-1} capacity at 120 *C*, while the KMnHCF electrode delivers 135 mAh g^{-1} at 10 *C* but only retains 41 mAh g^{-1} capacity at 120 *C*. Furthermore, the KFeMnHCF-3565 electrode exhibits a lower overpotential than the KMnHCF electrode (0.2 V versus 0.4 V) from 10 *C* to 120 *C*, also demonstrating its superior performance. It is worth noting that the KFeMnHCF-3565 cathode exhibits the highest capacity at rates of 0.5–120 *C* among all of the reported PBA materials in the aqueous $K^+/Na^+/H^+$-ion batteries, as illustrated in Fig. 2d (corresponding detailed parameters are listed in Supplementary Table 5)[8–10,14–20], demonstrating its excellent rate capability.

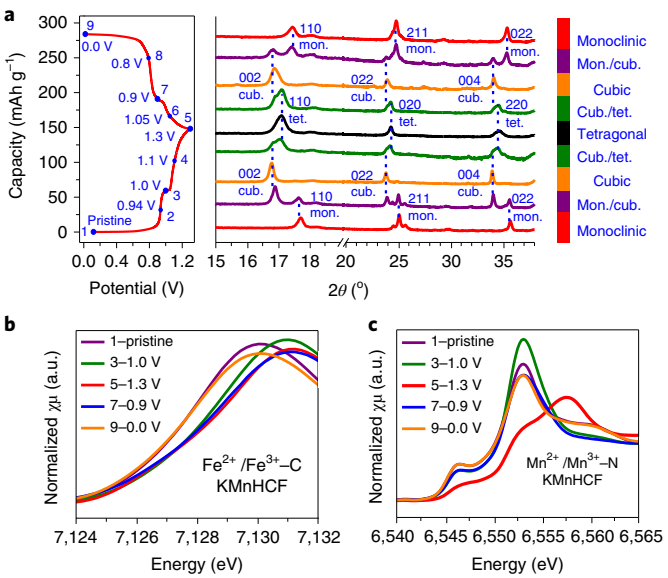

Fig. 3 | The structural evolution and charge compensation mechanism of the KMnHCF electrode. a, Ex situ XRD patterns of the KMnHCF electrode at different states during the first cycle. The blue dots marked from 1 to 9 in the charge–discharge curves (left) represent the states tested by ex situ XRD. **b**,**c**, XANES spectra of the KMnHCF electrode at different charge and discharge states for the Fe (**b**) and Mn K edges (**c**). $\chi\mu$ is the absorption coefficient of the X-ray. The states tested by XANES are marked by the blue dots (1, 3, 5, 7, 9) in the charge–discharge curves of **a**.

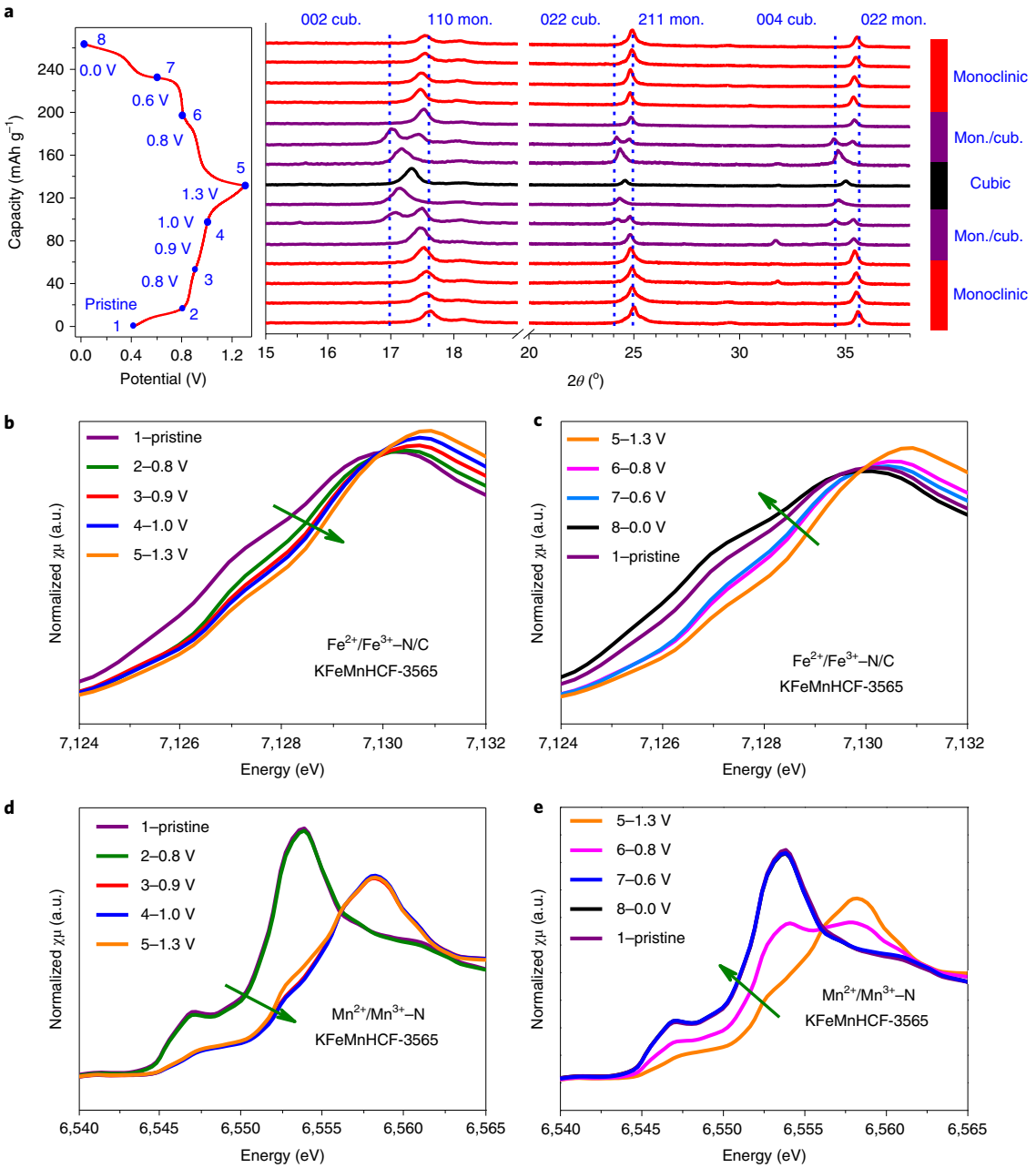

Fig. 4 | The structural evolution and charge compensation mechanism of the KFeMnHCF-3565 electrode. a, Ex situ XRD patterns of the KFeMnHCF-3565 electrode at different states during the first cycle. The blue dots marked from 1 to 8 in the charge–discharge curves (left) represent the states tested by XANES. **b**–**e**, XANES spectra of the KFeMnHCF-3565 electrode for the Fe K edge during charging (**b**), the Fe K edge during discharging (**c**), the Mn K edge during charging (**d**) and the Mn K edge during discharging (**e**). χμ is the absorption coefficient of the X-ray.

Furthermore, Fig. 2e shows the long-term cycling stability of the KFeMnHCF-3565 electrode, exhibiting a high capacity of 94 mAh g^{-1} at the ultrahigh rate of 100 *C* and 90% capacity retention over 10,000 cycles after experiencing a series of high-rate tests from 10 *C* to 120 *C*. Remarkably, even after 10,000 cycles at 100 *C*, the capacity can return to the value of 128 mAh g^{-1} when the current rate is set back to 10 *C*, demonstrating the robust structural stability. The 1st, 2nd and 10,330th charge–discharge curves are presented in Supplementary Fig. 6, exhibiting almost no decay in either capacity or voltage.

Storage mechanism of optimal cathode

To unravel the origin of the improved performance of the Fe-substituted Mn-rich PBA KFeMnHCF-3565 cathode, ex situ XRD, X-ray absorption near-edge spectroscopy (XANES) and first-principles calculations are performed. As shown in Fig. 3a, the KMnHCF electrode experiences two two-phase transitions (monoclinic to cubic and cubic to tetragonal phases), corresponding to the two voltage plateaus during the first cycle, which agrees with the behaviour reported previously in non-aqueous batteries[21]. Meanwhile, Fig. 3b,c shows the normalized XANES spectra of the Fe and Mn K edges for the KMnHCF electrode at different charge–discharge states (corresponding to the blue dots marked 1, 3, 5, 7 and 9 in the charge–discharge curves of Fig. 3a). During the first cycle of the KMnHCF electrode, the Fe K-edge peak only shifts up (0.1–1.0 V during the charging process) and back (0.9–0.0 V during the discharging process) at the lower voltage plateau while the

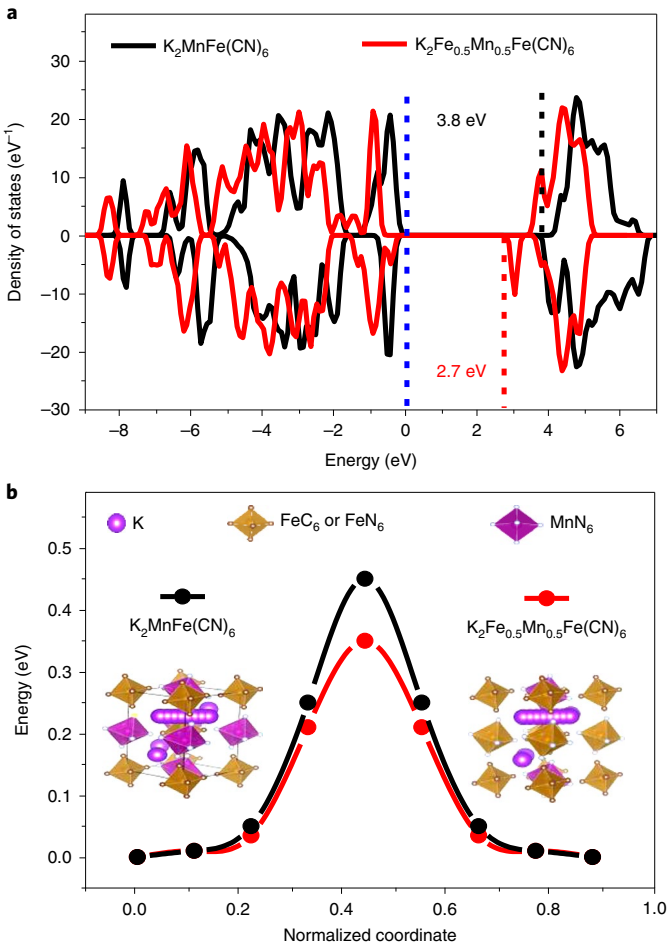

Fig. 5 | First-principles calculations. a, Density of states for the $K_2MnFe(CN)_6$ and Fe-substituted $K_2Fe_{0.5}Mn_{0.5}Fe(CN)_6$ model structures. The Fermi energy is set as zero. **b**, Migration energy barriers of the K^+-ion diffusion within the lattice of the $K_2MnFe(CN)_6$ and Fe-substituted $K_2Fe_{0.5}Mn_{0.5}Fe(CN)_6$ model structures. The insets show the calculated K^+ migration paths.

Mn K-edge peak shifts up (1.0–1.3 V during the charging process) and back (1.3–0.9 V during the discharging process) at the higher voltage plateau, indicating that the Fe^{2+}/Fe^{3+}–C and Mn^{2+}/Mn^{3+}–N redox reactions are almost independent and symmetric, which is consistent with previous reports in non-aqueous batteries[21,22].

In contrast, as shown in Fig. 4a, the KFeMnHCF-3565 electrode undergoes a solid solution reaction (0.4–0.95 V for charging and 0.8–0.0 V for discharging) and a phase transition between monoclinic and cubic phases (0.95–1.3 V for charging and 1.3-0.8 V for discharging). In addition, the normalized XANES spectra of KFeMnHCF-3565 samples (Fig. 4b–e, where the tested states are marked from 1 to 8 in the charge–discharge curves of Fig. 4a) demonstrate that the Fe K-edge peak shifts up and back during the whole charging (0.4–1.3 V) and discharging (1.3–0.0 V) processes. Note that the Fe substitution introduces a new Fe^{2+}/Fe^{3+}–N redox reaction, which can be speculated to occur between 0.4 and 0.8 V for charging and 0.6 and 0.0 V for discharging according to previous literature[10]. Therefore, the Fe^{2+}/Fe^{3+}–C redox reaction should occur at 0.8–1.3 V for charging and 1.3–0.6 V for discharging. Meanwhile, the XANES results prove that the Mn K-edge peak shifts up and back for specific charging (0.8–0.9 V) and discharging processes (1.3–0.6 V), demonstrating that the Mn^{2+}/Mn^{3+}–N redox reaction becomes asymmetric after Fe substitution. The detailed redox reaction processes of the KMnHCF and KFeMnHCF-3565 electrodes have been marked on the charge and discharge curves in Supplementary Fig. 7a,b.

The above analyses demonstrate that the Fe substitution leads to different structural evolutions and charge-transfer mechanisms between the KMnHCF and KFeMnHCF-3565 electrodes. In fact, the phase transition from the cubic to the tetragonal phases for the KMnHCF sample is related to the cooperative Jahn–Teller distortion of Mn^{3+} in the MnN_6 octahedron during the charging process according to previous literature[21,22]. Here, on the one hand, the Fe substitution can decrease the density of Mn^{3+} in the lattice, which is similar to the role of Fe/Co/Ni substitution in an Na-based Mn-rich PBA cathode[23]. On the other hand, the Fe substitution remarkably changes the mechanism of the Mn^{2+}/Mn^{3+}–N redox reaction. Owing to the above two roles, the Fe-substituted KFeMnHCF-3565 sample exhibits a mitigation of phase transitions, and thus displays a remarkably improved cycling stability.

Furthermore, the calculated results (Fig. 5a,b) prove that the Fe-substituted model structure ($K_2Fe_{0.5}Mn_{0.5}Fe(CN)_6$) has smaller band gap (2.7 eV versus 3.8 eV) and lower K^+-ion diffusion activation energy (0.35 eV versus 0.45 eV) than the model structure without Fe substitution ($K_2MnFe(CN)_6$), demonstrating that Fe substitution can effectively improve both electronic and K^+-ion conductivities. These advantages can account for the remarkably improved rate capability of the KFeMnHCF-3565 electrode compared with that of the KMnHCF electrode.

PTCDI anode in WIS electrolyte

After the optimization of the cathode, the exploration of a suitable anode is still necessary for a full AKIB. Here an organic PTCDI material with a monoclinic structure (space group *P*21/*n*) and rod-like morphology (Supplementary Fig. 8a,b), which exhibits good performance in an aqueous ammonium-ion battery[24], is chosen as the anode. Note that the PTCDI anode can reach lower redox potential in the 22 M KCF_3SO_3 electrolyte than in the 1 M KCF_3SO_3 electrolyte (−1.3 V versus −0.7 V, Supplementary Fig. 9a,b) without hydrogen evolution during the K^+ intercalation process at 0.5 *C*, owing to its wider voltage window, as shown in Fig. 6a. Meanwhile, the serious dissolution of the PTCDI anode during cycling in the dilute 1 M KCF_3SO_3 electrolyte is also inhibited when using 22 M KCF_3SO_3 electrolyte, which can be directly observed from the colour of the electrolytes after several cycles (pink in 1 M versus transparent in 22 M, insets of Supplementary Fig. 9a,b). The wide voltage window and dissolution-inhibiting property are related to the reduced amount of free water in concentrated electrolyte due to the strong K^+-solvation effect, as shown in Fig. 6b. The sharp peak at 3,531 cm^{-1} in the Raman spectra further demonstrates the strong K^+-solvation effect in the 22 M KCF_3SO_3 electrolyte, which is similar to phenomena in the Li-based WIS electrolyte[25].

As shown in Fig. 6c,d and Supplementary Fig. 10, the PTCDI anode exhibits superior rate capability at 0.5–20 *C* and delivers a high capacity of 125 mAh g^{-1} at 0.5 *C* and 110 mAh g^{-1} at 20 *C*, as well as excellent cycling stability, with 77% retention after 1,000 cycles at 20 *C* in the 22 M KCF_3SO_3 electrolyte.

It is worth noting that the remarkable rate capability and cycling stability of both the PTCDI anode and the KFeMnHCF-3565 cathode are not only attributable to the properties of the electrodes, but also benefit from the unique advantages of the 22 M KCF_3SO_3 WIS electrolyte. Among ACF_3SO_3-based (A: K, Na, Li) and other reported WIS electrolytes[11,25–27] (Fig. 6e, Supplementary Fig. 11a,b, Supplementary Table 6 and Supplementary Note 1), the highly concentrated 22 M KCF_3SO_3 electrolyte exhibits superior overall performance, including a wide voltage window (~3.0 V), high conductivity (76 mS cm^{-1} at 25 °C, 10 mS cm^{-1} at −20 °C) and low viscosity (6.5 mPa s at 25 °C), promising for enabling a superior-performance aqueous K-ion full battery.

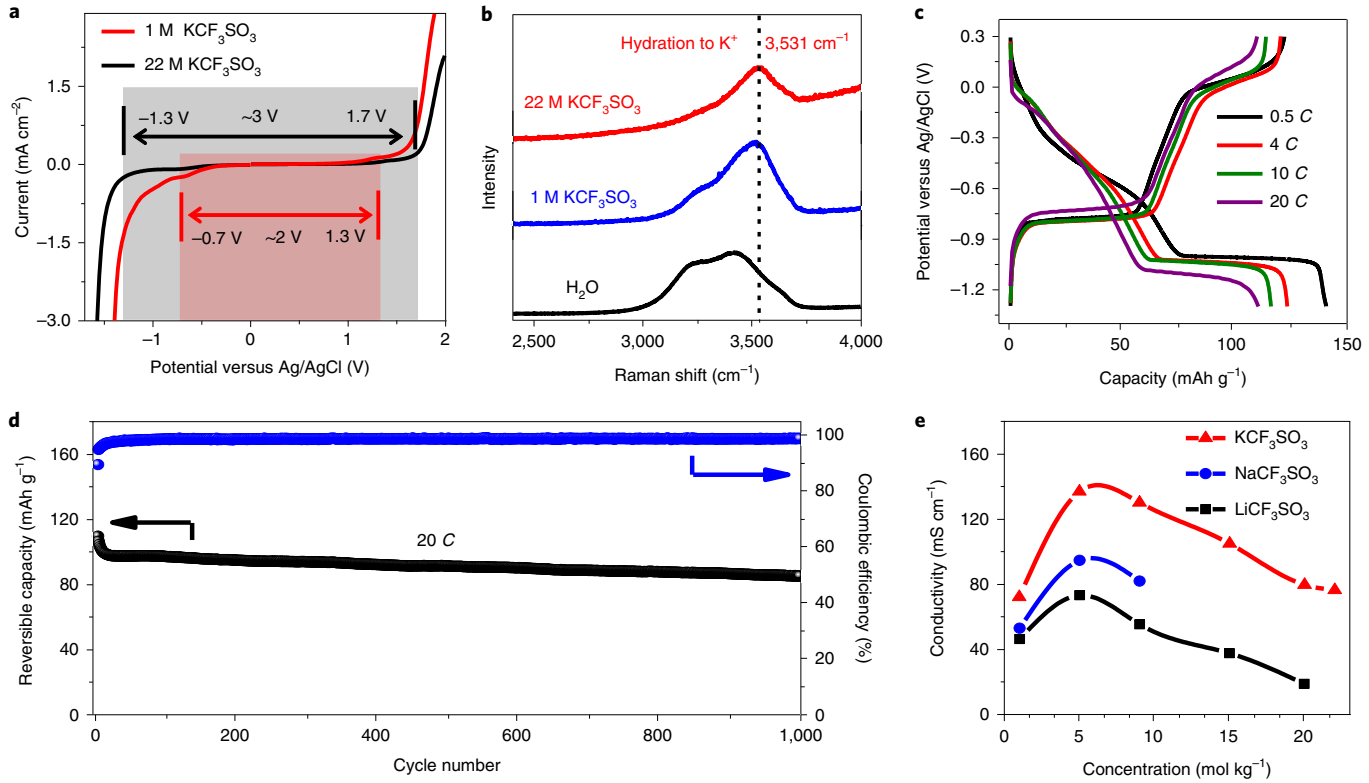

Fig. 6 | Performance of the WIS electrolyte and the PTCDI anode. a, Linear sweep voltammetry profiles recorded on titanium mesh at 10 mV s^{-1} in 1 M and 22 M KCF_3SO_3 electrolytes. The electrochemical stability window of the 1 M and 22 M KCF_3SO_3 electrolytes are marked with red and black, respectively. **b**, The Raman spectra of 1 M and 22 M KCF_3SO_3 electrolytes and H_2O observed in the range of 2,400–4,000 cm^{-1} correspond to the O–H stretching modes of water molecules. The sharp peaks at 3,531 cm^{-1} (black dashed line) are attributed to K^+-solvated water molecules that are not clustered through hydrogen bonding. **c**, Typical charge–discharge curves of the PTCDI anode at rates of 0.5 *C*, 4 *C*, 10 *C* and 20 *C* in the 22 M KCF_3SO_3 electrolyte, respectively (1 *C* = 0.13 A g^{-1}). **d**, Long-term cycling performance of the PTCDI anode at 20 *C* from −1.3 to 0.3 V (versus Ag/AgCl) in the 22 M KCF_3SO_3 electrolyte. **e**, Ionic conductivity versus concentration for $LiCF_3SO_3$-, $NaCF_3SO_3$- and KCF_3SO_3-based aqueous electrolytes at 25 °C.

Full AKIB

The combination of the Fe-substituted Mn-rich PBA cathode, organic PTCDI anode and concentrated electrolyte enables the assembly of the KFeMnHCF-3565//22 M KCF_3SO_3//PTCDI full AKIB. The 1st, 2nd, 100th, 200th, 400th and 500th charge–discharge curves at 4 *C* in Fig. 7a show that the full battery can stably operate between 0 V and 2.6 V. The full battery exhibits a high capacity of 63 mAh g^{-1} at low rate of 0.5 *C* (based on the mass of both cathode and anode) and an average voltage of 1.27 V, as well as a high capacity of 54 mAh g^{-1} at high rate of 20 *C* (Supplementary Fig. 12). The corresponding energy and power densities at 0.5–20 *C* are listed in Supplementary Table 7, indicating that the AKIB outputs an energy density of 80 Wh kg^{-1} at a power density of 41 W kg^{-1} and still holds an energy density of 67 Wh kg^{-1} at a power density of 1,612 W kg^{-1}.

Moreover, the full battery exhibits remarkable cycling stability, with capacity retention of 73% over 2,000 cycles at 4 *C*, as shown in Fig. 7c. We compared the performance of this full AKIB with previously reported aqueous Na-ion batteries as shown in Fig. 7b, it is clear that the proposed KFeMnHCF-3565//PTCDI full battery shows the best performance in terms of energy density, rate capability and cycling life (corresponding detailed parameters are listed in Supplementary Table 8)[17,18,28–33].

In addition, we also evaluated the electrochemical performance of an 11 mAh pouch cell at low rates (0.5 *C*/0.1 *C*) and low/high temperatures (−20 °C/−10 °C/25 °C/60 °C), as shown in Fig. 7d,e. The capacity at the low rate of 0.5 *C* is reduced from 11.1 mAh to 9.2 mAh when the temperature decreases from 25 °C to −10 °C. Subsequently, the capacity recovers to 10.7 mAh with the temperature increasing to 60 °C. Furthermore, the performance at a lower rate of 0.1 *C* is also tested for the pouch cell, demonstrating a capacity of 11 mAh at a temperature of 25 °C and remains at 9.8 mAh when the temperature drops to −10 °C. Even at a temperature of −20 °C, the pouch cell still maintains 8.4 mAh capacity. The Coulombic efficiency of the pouch cell at 0.5 *C* and 25 °C is 90% in the first cycle then increases to 95.7% in the third cycle. Owing to the effect of temperature, the Coulombic efficiency further increases to 99.6% at −10 °C and drops to 90.4% at 60 °C. When the rate decreases to 0.1 *C*, the Coulombic efficiency is 92.7% at 25 °C, and then increases to near 99.9% at both −10 °C and −20 °C. Furthermore, the self-discharge performance is also evaluated using the pouch cell, which experiences a small voltage decay initially and then retains a voltage of about 1.8 V for 40 h (Supplementary Fig. 13).

Opportunities and challenges of AKIB

The proposed AKIB has some unique features and advantages. First, both cathode and anode are low-cost materials. The designed cathode consists of non-toxic and abundant elements and the room-temperature synthetic process is very simple and straightforward. The PTCDI anode is commercially available due to its application in the field of decorative paints. Second, both cathode and anode possess high capacity, superior rate capability and cycling stability. Here we adopt Fe substitution in a K-based Mn-rich PBA cathode to improve the rate capability and inhibit the cubic to tetragonal phase transition during cycling, which successfully demonstrates a

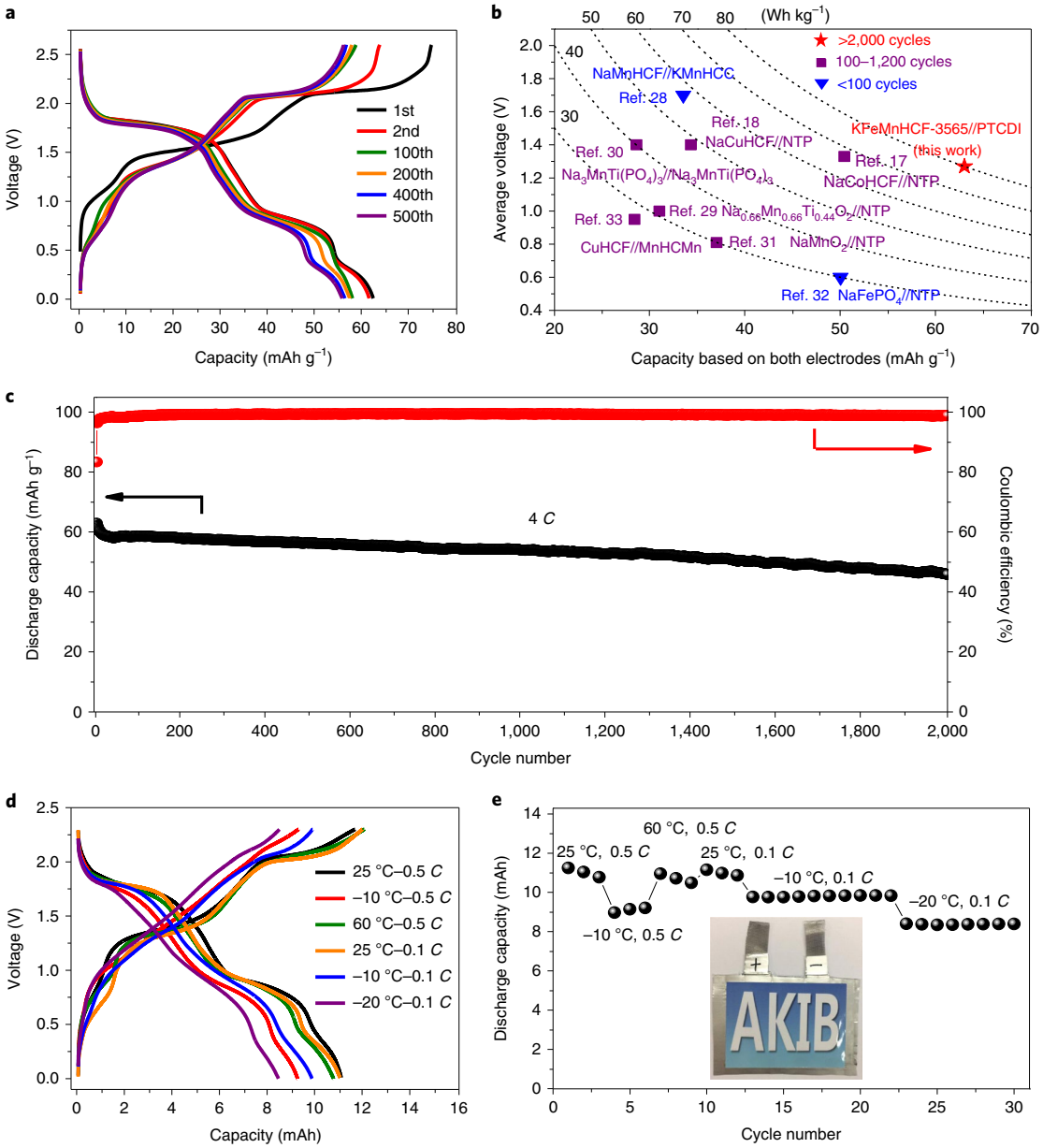

Fig. 7 | Performance of the KFeMnHCF-3565//22 M KCF_3SO_3//PTCDI full battery. a, Charge–discharge curves of 1st, 2nd, 100th, 200th, 400th and 500th cycles for coin cells at 4 *C* from 0 V to 2.6 V (1 *C* = 0.13 A g^{-1}). **b**, Comparison of average voltage, capacity based on total mass of both electrodes, lifespan and energy density for the full battery with reported aqueous Na-ion full batteries. **c**, Long-term cycling performance of the coin cell at 4 *C*. **d**,**e**, Performance of the KFeMnHCF-3565//22 M KCF_3SO_3//PTCDI pouch cell at different rates (0.5/0.1 C) and temperatures (−20/−10/25/60 °C) from 0 V to 2.3 V for typical charge–discharge curves (**d**) and the cycling performance (**e**). The inset of **e** displays an optical photograph of the assembled AKIB pouch cell.

high capacity of 135 mAh g^{-1}, superior rate capability (70% capacity retention at 100 *C*) and excellent cycling stability with 90% capacity retention over 10,000 cycles. We also use the organic PTCDI material as the anode for the AKIB, which exhibits a high capacity of 125 mAh g^{-1} at 0.5 *C* and excellent rate capability with 110 mAh g^{-1} at 20 *C*, as well as superior cycling stability with 77% capacity retention after 1,000 cycles at 20 *C*. Third, the 22 M KCF_3SO_3 electrolyte with minimum free water exhibits a wide voltage window of 3 V, which can not only inhibit the dissolution of both cathode and anode during cycling to ensure the full battery's superior cycling stability but also enable the full battery to operate above 2 V at the low rate of 0.1 *C*. Fourth, the 22 M KCF_3SO_3 electrolyte possesses high K^+-ion conductivity at both room temperature and low temperature (76 mS cm^{-1} at 25 °C, 10 mS cm^{-1} at −20 °C), enabling a superior wide temperature (−20 °C to 60 °C) performance. The assembled 11 mAh pouch cell proves that the system can still retain 76% of its capacity at 0.1 *C* when the temperature drops from 25 °C to −20 °C. Fifth, the synergistic effect from the whole system contributes to the remarkable performance of the AKIB, which exhibits a high energy density of 80 Wh kg^{-1} and an excellent cycling stability with 73% capacity retention over 2,000 cycles at 4 *C*, surpassing the performance of reported aqueous Na-ion batteries.

In view of the above advantages, the proposed AKIB is a promising candidate for practical application in grid energy storage. The parameters of our AKIB in comparison with other electrochemical technologies for grid energy storage systems are listed in Supplementary Table 9 (refs. [1,34–42]), indicating that the energy density of our AKIB is much higher than that of supercapacitors

and comparable with the lead–acid and vanadium redox-based flow batteries (the real energy density of the KFeMnHCF-3565//PTCDI full battery in the application scenarios is estimated by halving the corresponding value calculated based on the total mass of cathode and anode). Moreover, our AKIB surpasses Li-ion batteries in terms of safety and toxicity, and is better than the Na–S battery in terms of acceptable operating temperature range. Furthermore, the key elemental abundance of our AKIB materials in the Earth's crust is much higher than those of Ni–MH, lead–acid, Li-ion and vanadium redox-based flow batteries, indicating the potential advantages in terms of cost reduction and large-scale applications.

In spite of these advantages, there is still room for improvement of the present battery prototype in the future to promote its practical applications. First, for the electrode materials, even if the Fe-substituted Mn-rich PBA cathode seems the optimal choice, the anode side still needs further optimization, where materials with higher capacity and lower redox potential could further increase the energy density of AKIBs. Given the above considerations, organic materials will be promising candidates due to the characteristics of achievable multi-electron reactions and adjustable redox potential[43,44]. Second, the cost of the concentrated electrolyte used in the full battery may be one of the main concerns for practical applications in the future. In fact, this is commonly the main challenge in WIS electrolyte-based batteries. To decrease the cost of the full battery while ensuring its superior low-rate performance and high operating voltage, great efforts should be made to explore cheaper salts with high solubility, decrease the electrolyte concentration by modifying the interface, or employ a hybrid aqueous–non-aqueous solvent and so on.

Conclusions

In summary, we have developed an aqueous K-ion full battery, which was assembled from an Fe-substituted Mn-rich PBA cathode, 22 M KCF_3SO_3 WIS electrolyte and PTCDI organic anode. The $K_{1.85}Fe_{0.33}Mn_{0.67}[Fe(CN)_6]_{0.98}{\cdot}0.77H_2O$ cathode exhibits an unprecedented performance of high capacity, 135 mAh g^{-1} at 0.5 *C* and 94 mAh g^{-1} at 100 *C*, with a capacity retention of 90% over 10,000 cycles in the 22 M KCF_3SO_3 WIS electrolyte. The ex situ XRD and XANES results together with first-principles calculations reveal that the Fe-substitution strategy not only decreases the band gap and K^+-ion diffusion activation energy but also inhibits the formation of tetragonal phase at the end of the charging process, which greatly improves the rate capability and cycling stability. Moreover, benefiting from the synergistic contribution of the organic PTCDI anode with high capacity (125 mAh g^{-1}), and the 22 M KCF_3SO_3 WIS electrolyte with wide voltage window (3 V), dissolution-inhibiting effect and high conductivity (76 mS cm^{-1} at 25 °C, 10 mS cm^{-1} at −20 °C), the full battery achieves a high energy density of 80 Wh kg^{-1} and excellent cycling stability, with 73% capacity retention over 2,000 cycles at 4 *C*. Furthermore, the 11 mAh pouch cell demonstrates superior performance at low rates (0.5 *C*/0.1 *C*) and low/high temperatures (−20 °C/−10 °C/25 °C/60 °C). This work represents an important step towards developing AKIBs and opens up a promising prospect for grid-scale energy storage.

Methods

Materials synthesis. $K_xFe_yMn_{1-y}[Fe(CN)_6]_w{\cdot}zH_2O$ ($y=0$, 0.2, 0.35, 0.5) samples were prepared by a simple precipitation method. Typically, 2 mmol $K_4Fe(CN)_6{\cdot}3H_2O$ and corresponding proportions of $FeSO_4{\cdot}7H_2O$ and $MnSO_4{\cdot}H_2O$ were dissolved in 100 ml and 80 ml saturated KCl solution, respectively. Then, the latter solution was slowly dropped into the former with magnetic stirring at 60 °C. After 12 h, the formed precipitate was centrifuged and washed thoroughly with deionized water. Finally, the product was obtained after drying under air at 80 °C for 12 h. The PTCDI was purchased from Alfa.

Electrochemical measurements. Composite electrodes were fabricated by compressing active materials, carbon black and poly(vinylidene difluoride) at a weight ratio of 7:2:1 on titanium mesh. The three-electrode cell for the cathodes consisted of $K_xFe_yMn_{1-y}[Fe(CN)_6]_w{\cdot}zH_2O$ composite (5.8 mg cm^{-2}) as the working electrode, activated carbon as the counterelectrode and Ag/AgCl as the reference electrode. The anode three-electrode cell for the PTCDI consisted of composites (5.2 mg cm^{-2}) as the working electrode, activated carbon as the counterelectrode and Ag/AgCl as the reference electrode. The typical three-electrode cell we used is shown in Supplementary Fig. 14. For the coin cells, the current collectors were Ti mesh. The mass ratio of KFeMnHCF-3565/PTCDI is 1/0.9 (1 $C=0.13$ A g^{-1}), the mass loading of the KFeMnHCF-3565 cathode is 5.8 mg cm^{-2} and the mass loading of the PTCDI anode is 5.2 mg cm^{-2}. For the pouch cell, the mass ratio of KFeMnHCF-3565/PTCDI is 1/0.92 (1 $C=0.13$ A g^{-1}), the current collectors are Ti mesh, the mass loading of the KFeMnHCF-3565 cathode is 15 mg cm^{-2} and the mass loading of the PTCDI anode is 11 mg cm^{-2}. 22 M KCF_3SO_3 represents the solution obtained by dissolving 22 mol KCF_3SO_3 salt in 1 l water.

Materials characterization. The structure was characterized using an X'Pert Pro MPD X-ray diffractometer (D8 Bruker) with Cu Kα radiation ($\lambda=1.5405$ Å) in a scan range (2θ) of 10–80°. The samples for ex situ XRD were prepared in the three-electrode cell, washed in alcohol and then sealed in a valve bag. The morphologies of the cathodes were investigated by scanning electron microscopy (Hitachi S-4800). The transmission electron microscopy images of the cathode are obtained with a JEOL 2100F field emission microscope. The specific ratios of K, Fe and Mn in the cathodes were measured by inductively coupled plasma atomic emission spectrometry. The water content of samples was estimated by thermogravimetric analysis. Linear sweep voltammetry was carried out using a CHI 660E electrochemical work station. The Raman spectra for electrolytes were collected with an NRS-5100 spectrometer (JASCO) using using a 532 nm diode-pumped solid-state laser between 1,200 and 100 cm^{-1}. Each electrolyte solution was placed in a quartz cell, and the laser was directed through the quartz crystal window. Ex situ hard X-ray absorption spectroscopy (hXAS) experiments were performed at beamline X18A of the National Synchrotron Light Source in Brookhaven National Laboratory and the Shanghai Synchrotron Radiation Facility (Shanghai, China) in transmission mode with a Si(111) double-crystal monochromator detuned to 35–50% of its original maximum intensity to eliminate the higher-order harmonics. The reference spectrum was simultaneously collected for energy calibration using a reference metal foil. The XANES spectra were analysed with the ATHENA software package[45].

Computation. First-principles calculations are performed with the Vienna ab initio simulation package (VASP)[46]. The present data are obtained using the spin-polarized generalized gradient approximation (GGA) with a parameterized exchange–correlation functional according to Perdew, Burke and Ernzerhof[47]. The K 2*p*, 3*s*, Mn 3*d*, 4*s*, Fe 3*d*, 4*s* and O 2*s*, 2*p* orbitals are treated as valence states. The Hubbard parameter (GGA + *U*) is applied to correct the incomplete cancellation of the self-interaction effect of the GGA method[48]. The effective single parameters of *U*–*J* for Mn and Fe are 5.0 eV and 4.3 eV, respectively, according to preview literature[49]. For all calculations the cut-offs of the wave function are 520 eV. The energy and force convergence criteria are 10^{-6} eV and 0.01 eV $Å^{-1}$, respectively. The calculations for electronic structures and the nudged elastic band were performed with ($a\times b\times c$) supercells (including 32 atoms in total) for both $K_2MnFe(CN)_6$ and $K_2Fe_{0.5}Mn_{0.5}Fe(CN)_6$.

Data availability

The data that support the plots within this paper and other findings of this study are available from the corresponding author on reasonable request.

Received: 10 September 2018; Accepted: 8 April 2019;
Published online: 13 May 2019

References

1. Yang, Z. et al. Electrochemical energy storage for green grid. *Chem. Rev.* **111**, 3577–3613 (2011).
2. Dunn, B., Kamath, H. & Tarascon, J.-M. Electrical energy storage for the grid: a battery of choices. *Science* **334**, 928–935 (2011).
3. Kim, H. et al. Aqueous rechargeable Li and Na ion batteries. *Chem. Rev.* **114**, 11788–11827 (2014).
4. Eftekhari, A., Jian, Z. & Ji, X. Potassium secondary batteries. *ACS Appl. Mater. Interfaces* **9**, 4404–4419 (2017).
5. Kim, H. et al. Recent progress and perspective in electrode materials for K-ion batteries. *Adv. Energy Mater.* **8**, 1702384 (2018).
6. Kubota, K., Dahbi, M., Hosaka, T., Kumakura, S. & Komaba, S. Towards K-ion and Na-ion batteries as "beyond Li-ion". *Chem. Rec.* **18**, 459–479 (2018).
7. Qian, J. et al. Prussian blue cathode materials for sodium-ion batteries and other ion batteries. *Adv. Energy Mater.* **8**, 1702619 (2018).
8. Wessells, C. D., Peddada, S. V., Huggins, R. A. & Cui, Y. Nickel hexacyanoferrate nanoparticle electrodes for aqueous sodium and potassium ion batteries. *Nano Lett.* **11**, 5421–5425 (2011).
9. Wessells, C. D., Huggins, R. A. & Cui, Y. Copper hexacyanoferrate battery electrodes with long cycle life and high power. *Nat. Commun.* **2**, 550 (2011).

10. Su, D., McDonagh, A., Qiao, S. Z. & Wang, G. High-capacity aqueous potassium-ion batteries for large-scale energy storage. *Adv. Mater.* **29**, 1604007 (2017).
11. Suo, L. et al. "Water-in-salt" electrolyte enables high-voltage aqueous lithium-ion chemistries. *Science* **350**, 938–943 (2015).
12. Leonard, D. P., Wei, Z., Chen, G., Du, F. & Ji, X. Water-in-salt electrolyte for potassium-ion batteries. *ACS Energy Lett.* **3**, 373–374 (2018).
13. Liu, Y., Wei, G., Ma, M. & Qiao, Y. Role of acid in tailoring prussian blue as cathode for high-performance sodium-ion battery. *Chem* **23**, 15991–15996 (2017).
14. Wu, X. et al. Diffusion-free Grotthuss topochemistry for high-rate and long-life proton batteries. *Nat. Energy* **4**, 123–130 (2019).
15. Ren, W., Chen, X. & Zhao, C. Ultrafast aqueous potassium-ion batteries cathode for stable intermittent grid-scale energy storage. *Adv. Energy Mater.* **8**, 1801413 (2018).
16. Nakamoto, K., Sakamoto, R., Ito, M., Kitajou, A. & Okada, S. Effect of concentrated electrolyte on aqueous sodium-ion battery with sodium manganese hexacyanoferrate cathode. *Electrochemistry* **85**, 179–185 (2017).
17. Wu, X. et al. Vacancy-free prussian blue nanocrystals with high capacity and superior cyclability for aqueous sodium-ion batteries. *ChemNanoMat* **1**, 188–193 (2015).
18. Wu, X. Y. et al. Energetic aqueous rechargeable sodium-ion battery based on $Na_2CuFe(CN)_6$-$NaTi_2(PO_4)_3$ intercalation chemistry. *ChemSusChem* **7**, 407–411 (2014).
19. Wu, X., Cao, Y., Ai, X., Qian, J. & Yang, H. A low-cost and environmentally benign aqueous rechargeable sodium-ion battery based on $NaTi_2(PO_4)_3$–$Na_2NiFe(CN)_6$ intercalation chemistry. *Electrochem. Commun.* **31**, 145–148 (2013).
20. Wu, X. Y. et al. Low-defect Prussian blue nanocubes as high capacity and long life cathodes for aqueous Na-ion batteries. *Nano Energy* **13**, 117–123 (2015).
21. Bie, X., Kubota, K., Hosaka, T., Chihara, K. & Komaba, S. A novel K-ion battery: hexacyanoferrate(II)/graphite cell. *J. Mater. Chem. A* **5**, 4325–4330 (2017).
22. Xue, L. et al. Low-cost high-energy potassium cathode. *J. Am. Chem. Soc.* **139**, 2164–2167 (2017).
23. Moritomo, Y., Urase, S. & Shibata, T. Enhanced battery performance in manganese hexacyanoferrate by partial substitution. *Electrochim. Acta* **210**, 963–969 (2016).
24. Wu, X. et al. Rocking-chair ammonium-ion battery: a highly reversible aqueous energy storage system. *Angew. Chem. Int. Ed.* **56**, 13026–13030 (2017).
25. Yamada, Y. et al. Hydrate-melt electrolytes for high-energy-density aqueous batteries. *Nat. Energy* **1**, 16129 (2016).
26. Lukatskaya, M. R. et al. Concentrated mixed cation acetate "water-in-salt" solutions as green and low-cost high voltage electrolytes for aqueous batteries. *Energy Environ. Sci.* **11**, 2876–2883 (2018).
27. Suo, L. et al. Advanced high-voltage aqueous lithium-ion battery enabled by "water-in-bisalt" electrolyte. *Angew. Chem. Int. Ed.* **55**, 7136–7141 (2016).
28. Nakamoto, K., . & Sakamoto, R. & Sawada, Y. & Ito, M. & Okada, S. Over 2 V aqueous sodium-ion battery with prussian blue-type electrodes. *Small Methods* **3**, 1800220 (2019).
29. Suo, L. et al. "Water-in-salt" electrolyte makes aqueous sodium-ion battery safe, green, and long-lasting. *Adv. Energy Mater.* **7**, 1701189 (2017).
30. Gao, H. & Goodenough, J. B. An aqueous symmetric sodium-ion battery with NASICON-structured $Na_3MnTi(PO_4)_3$. *Angew. Chem. Int. Ed.* **55**, 12768–12772 (2016).
31. Hou, Z., Li, X., Liang, J., Zhu, Y. & Qian, Y. An aqueous rechargeable sodium ion battery based on a $NaMnO_2$–$NaTi_2(PO_4)_3$ hybrid system for stationary energy storage. *J. Mater. Chem. A* **3**, 1400–1404 (2015).
32. Fernández-Ropero, A. J., Saurel, D., Acebedo, B., Rojo, T. & Casas-Cabanas, M. Electrochemical characterization of $NaFePO_4$ as positive electrode in aqueous sodium-ion batteries. *J. Power Sources* **291**, 40–45 (2015).
33. Pasta, M. et al. Full open-framework batteries for stationary energy storage. *Nat. Commun.* **5**, 3007 (2014).
34. Kumar, D., Rajouria, S. K., Kuhar, S. B. & Kanchan, D. K. Progress and prospects of sodium-sulfur batteries: a review. *Solid State Ion.* **312**, 8–16 (2017).
35. Hesse, H., Schimpe, M., Kucevic, D. & Jossen, A. Lithium-ion battery storage for the grid—a review of stationary battery storage system design tailored for applications in modern power grids. *Energies* **10**, 2107 (2017).
36. Opiyo, N. Energy storage systems for PV-based communal grids. *J. Energy Storage* **7**, 1–12 (2016).
37. Hueso, K. B., Armand, M. & Rojo, T. High temperature sodium batteries: status, challenges and future trends. *Energy Environ. Sci.* **6**, 734 (2013).
38. Díaz-González, F., Sumper, A., Gomis-Bellmunt, O. & Villafáfila-Robles, R. A review of energy storage technologies for wind power applications. *Renew. Sustain. Energy Rev.* **16**, 2154–2171 (2012).
39. Soloveichik, G. L. Battery technologies for large-scale stationary energy storage. *Annu. Rev. Chem. Biomol. Eng.* **2**, 503–527 (2011).
40. Fetcenko, M. A. et al. Recent advances in NiMH battery technology. *J. Power Sources* **165**, 544–551 (2007).
41. Yabuuchi, N., Kubota, K., Dahbi, M. & Komaba, S. Research development on sodium-ion batteries. *Chem. Rev.* **114**, 11636–11682 (2014).
42. Pan, H. L., Hu, Y. S. & Chen, L. Q. Room-temperature stationary sodium-ion batteries for large-scale electric energy storage. *Energy Environ. Sci.* **6**, 2338–2360 (2013).
43. Liang, Y. et al. Universal quinone electrodes for long cycle life aqueous rechargeable batteries. *Nat. Mater.* **16**, 841–848 (2017).
44. Lee, M. et al. High-performance sodium–organic battery by realizing four-sodium storage in disodium rhodizonate. *Nat. Energy* **2**, 861–868 (2017).
45. Ravel, B. & Newville, M. ATHENA, ARTEMIS, HEPHAESTUS: data analysis for X-ray absorption spectroscopy using IFEFFIT. *J. Synchrotron Radiat.* **12**, 537–541 (2005).
46. Kresse, G. & Furthmuller, J. Efficient iterative schemes for ab initio total-energy calculations using a plane-wave basis set. *Phys. Rev. B* **54**, 11169–11186 (1996).
47. Perdew, J. P., Burke, K. & Ernzerhof, M. Generalized gradient approximation made simple. *Phys. Rev. Lett.* **77**, 3865–3868 (1996).
48. Anisimov, V. I., Zaanen, J. & Andersen, O. K. Band theory and Mott insulators—Hubbard U instead of Stoner I. *Phys. Rev. B* **44**, 943–954 (1991).
49. Xiao, P., Song, J., Wang, L., Goodenough, J. B. & Henkelman, G. Theoretical study of the structural evolution of a $Na_2FeMn(CN)_6$ cathode upon Na intercalation. *Chem. Mater.* **27**, 3763–3768 (2015).

Acknowledgements

This work was supported by the National Natural Science Foundation of China (51725206 and 51421002), the National Key Technologies R&D Programme of China (2016YFB0901500), and the Strategic Priority Research Programme of the Chinese Academy of Sciences (XDA21070500), the Strategic Priority Research Programme of the Chinese Academy of Sciences (XDA21070500) and the Beijing Municipal Science and Technology Commission (Z181100004718008).

Author contributions

Y.-S.H. and Y.L. designed this work; L.J. synthesized the cathodes and carried out the electrochemical experiments and first-principles calculations; C.Z. performed the structural refinement, L.L. carried out the Raman test, J. Zhang and X.Y. performed the hXAS test; Q.Z. performed the transmission electron microscopy test, X.S. and J. Zhao performed the inductively coupled plasma test. L.J., Y.L. and Y.-S.H. wrote the paper; all of the authors participated in analysis of the experimental data and discussions of the results as well as preparing the paper.

Competing interests

The authors declare no competing interests.

Additional information

Supplementary information is available for this paper at https://doi.org/10.1038/s41560-019-0388-0.

Reprints and permissions information is available at www.nature.com/reprints.

Correspondence and requests for materials should be addressed to Y.L. or Y.-S.H.

Publisher's note: Springer Nature remains neutral with regard to jurisdictional claims in published maps and institutional affiliations.